

The *Gaia*-ESO survey: a lithium depletion boundary age for NGC 2232

A. S. Binks¹,^{*} R. D. Jeffries¹, R. J. Jackson,¹ E. Franciosini², G. G. Sacco,² A. Bayo^{3,4},
L. Magrini,² S. Randich,² J. Arancibia-Silva,^{3,4} M. Bergemann,⁵ A. Bragaglia,⁶ G. Gilmore,⁷ A. Gonneau,⁷
A. Hourihane,⁷ P. Jofré,⁸ A. J. Korn,⁹ L. Morbidelli,² L. Prisinzano,¹⁰ C. C. Worley⁷ and S. Zaggia¹¹

¹*Astrophysics Group, School of Chemical and Physical Sciences, Keele University, Keele, ST5 5BG, United Kingdom*

²*INAF-Osservatorio Astrofisico di Arcetri, Largo E. Fermi, 5, I-50125 Firenze, Italy*

³*Instituto de Física y Astronomía, Facultad de Ciencias, Universidad de Valparaíso, Av. Gran Bretaña 1111, Valparaíso, Chile*

⁴*Núcleo Milenio de Formación Planetaria - NPF, Universidad de Valparaíso, Av. Gran Bretaña 1111, Valparaíso, Chile*

⁵*Max-Planck Institut für Astronomie, Königstuhl 17, D-69117 Heidelberg, Germany*

⁶*INAF-Osservatorio di Astrofisica e Scienza dello Spazio via Gobetti 93/3, I-40129 Bologna, Italy*

⁷*Institute of Astronomy, University of Cambridge, Madingley Road, Cambridge CB3 0HA, UK*

⁸*Núcleo de Astronomía, Facultad de Ingeniería y Ciencias, Universidad Diego Portales (UDP), Santiago de Chile*

⁹*Observational Astrophysics, Division of Astronomy and Space Physics, Department of Physics and Astronomy, Uppsala University, Box 516, SE-751 20 Uppsala, Sweden*

¹⁰*INAF-Osservatorio Astronomico di Palermo, Piazza del Parlamento, 1, 90134 Palermo, Italy*

¹¹*INAF-Osservatorio Astronomico di Padova, vicolo dell'Osservatorio, 5, I-35122 Padova, Italy*

Accepted 2021 May 3. Received 2021 May 3; in original form 2021 April 6

ABSTRACT

Astrometry and photometry from *Gaia* and spectroscopic data from the *Gaia*-ESO Survey (GES) are used to identify the lithium depletion boundary (LDB) in the young cluster NGC 2232. A specialized spectral line analysis procedure was used to recover the signature of undepleted lithium in very low luminosity cluster members. An age of 38 ± 3 Myr is inferred by comparing the LDB location in absolute colour–magnitude diagrams (CMDs) with the predictions of standard models. This is more than twice the age derived from fitting isochrones to low-mass stars in the CMD with the same models. Much closer agreement between LDB and CMD ages is obtained from models that incorporate magnetically suppressed convection or flux-blocking by dark, magnetic starspots. The best agreement is found at ages of 45–50 Myr for models with high levels of magnetic activity and starspot coverage fractions >50 per cent, although a uniformly high spot coverage does not match the CMD well across the full luminosity range considered.

Key words: stars: kinematics and dynamics – stars: late-type – stars: pre-main-sequence – solar neighbourhood.

1 INTRODUCTION

Estimating the ages of stars and star clusters is of great importance in astrophysics, but age is something which cannot directly be measured (Soderblom 2010). Star clusters, with their populations of nearly coeval stars of similar initial compositions but with a broad range of masses, offer the most incisive tests of stellar physics and a route towards establishing the time-dependence of physical processes associated with star formation and stellar evolution, and a means of calibrating secondary age indicators [e.g. rotation and abundance ratios; see e.g. Casali et al. (2019, 2020)] that can be applied to more general galactic populations.

A fundamental test of stellar models that can be applied very effectively in star clusters is that ages derived from multiple methods, that are sensitive to different aspects of stellar physics or that sample different parts of the stellar mass spectrum, should agree. In the realm of young stars, there has been growing disquiet that ages determined from high-mass stars evolving on and away from the

main sequence are systematically older (by factors of two in the youngest clusters) than the ages determined from fitting isochrones in colour–magnitude diagrams (CMDs) for low-mass pre main sequence (PMS) stars in the same clusters (Lyra et al. 2006; Naylor 2009; Bell et al. 2013; Herczeg & Hillenbrand 2015; Feiden 2016).

Further indications of significant problems in the physics of low-mass PMS stars come from discrepancies between isochronal ages and the amount (and dispersion) of lithium that PMS stars deplete as they contract and their cores become hot enough to ‘burn’ lithium (Jeffries et al. 2017; Bouvier et al. 2018). There are also direct and indirect indications that magnetically active stars, whether they are fast-rotating and young or members of close, tidally locked binary systems, have larger radii than predicted by the most commonly used stellar models (Morales et al. 2009; Torres 2013; Malo et al. 2014b; Kraus et al. 2015, 2017; Rizzuto et al. 2020). This has led to suggestions that rotation, magnetic fields, and high surface coverage of starspots may significantly alter the evolutionary tracks and isochrones in young clusters (Feiden & Chaboyer 2013; Jackson & Jeffries 2014a; Somers & Pinsonneault 2015; MacDonald & Mullan 2017). If so, this would lead to an underestimate of young cluster ages by factors of ~ 2 and a significant underestimate of stellar masses,

* E-mail: alex.s.binks@gmail.com

particularly at low masses, when models that neglect these effects are adopted (e.g. Feiden 2016; Jeffries et al. 2017; MacDonald & Mullan 2021).

Resolving the age discrepancies in young clusters is crucial to correctly infer the properties and evolutionary processes of several strongly accreting stars identified at relatively late stages of their PMS, for example, TW Hydrae and Hen 3-600A (Muzerolle et al. 2000, Ronco et al. in preparation), dozens of accreting low-mass stars in Upper Scorpius (Manara et al. 2020), and many more ‘classical’ > 10 Myr old accretors identified in young stellar groups (Haisch, Lada & Lada 2001; Mamajek et al. 2004; De Marchi et al. 2013; Beccari et al. 2017; Silverberg et al. 2020).

Choosing which models and age scales to adopt is difficult because most age determination methods still have significant physical uncertainties associated with them; for example, the treatment of convection, the amount of core-overshooting, and the lack of a detailed understanding of how rotation and magnetic fields influence the stellar structure. It is not clear that any of the ages discussed above are correct!

Most weight should be attached to methods with the least model-dependence and the ‘lithium depletion boundary’ (LDB) technique is presently the least model-sensitive of those available (Soderblom et al. 2013). When low-mass, fully-convective PMS stars contract, their initial Li content is rapidly consumed once their cores reach $\sim 3 \times 10^6$ K because of the steep temperature dependence of the ${}^7\text{Li}(p,\alpha){}^4\text{He}$ reaction. More massive PMS stars reach this point more rapidly and the efficiency of convective mixing ensures that this is reflected in their photospheric Li abundance shortly afterwards (e.g. Bildsten et al. 1997). The net effect is that in a cluster of stars with a range of masses, there is predicted to be a sharp transition, the LDB, between stars that have depleted all of their Li and those with only slightly lower masses and luminosities that still retain all their initial Li. The sharpness of this transition persists even after accounting for the known Li dispersion for a given mass/ T_{eff} bin.

The luminosity at the LDB therefore has the potential to be a precise age indicator but it is also likely to be accurate. Theoretical parameter studies have varied physical inputs over the range of their remaining uncertainties and found that LDB ages are unlikely to change by more than about 10 per cent at the youngest ages for which the technique is viable and just a few per cent at older ages (Burke, Pinsonneault & Sills 2004; Tognelli, Prada Moroni & Degl’Innocenti 2015). Even the adoption of models that incorporate magnetic activity and radius inflation, which can increase isochronal ages by a factor of 2, result in systematic LDB age increases of just 10–20 per cent in young groups, as predicted by models accounting for the effects of starspots (Jackson & Jeffries 2014b; Somers & Pinsonneault 2015), and supported by LDB analyses of young groups, e.g. the β Pictoris Moving Group (21–26 Myr; Binks & Jeffries 2016).

LDB ages have been established in only about a dozen young clusters and associations with ages between about 20 and 700 Myr (see Jeffries et al. 2013; Soderblom et al. 2013; Martín et al. 2018, and references therein). The method requires an assessment of the Li abundances in very low-mass, low luminosity cluster M-dwarfs and thus large amounts of spectroscopic time on large telescopes. Nevertheless, the results are extremely valuable; obtaining a densely sampled set of LDB age determinations in the age range where it is sensitive can identify deficiencies in stellar models and empirically calibrate evolutionary time-scales for contracting PMS stars.

Current results indicate that LDB ages are usually older than those obtained by isochrone fitting (Stauffer, Schultz & Kirkpatrick 1998; Stauffer et al. 1999; Jeffries & Oliveira 2005; Jeffries et al. 2013;

Binks & Jeffries 2014; Malo et al. 2014a). This suggests: (i) that high-mass stellar models need to incorporate modest levels of convective core overshoot and/or rotational mixing to provide matched main sequence turn-off ages; and (ii) that standard low-mass isochronal ages may need revising upwards by incorporating new physics into the PMS modelling.

In this paper we report a new LDB age determination for the young cluster NGC 2232, using spectroscopy obtained as part of the Gaia-ESO spectroscopic survey (Gilmore et al. 2012; Randich, Gilmore & Gaia-ESO Consortium 2013, hereafter GES). With an age of ~ 30 Myr, NGC 2232 is at an interesting stage in its evolution where ages can be estimated from isochronal fits to both low- and high-mass stars as well as the LDB. The technique for selecting NGC 2232 members is described in Section 2, while Section 3 explains the method for estimating the relative Li content of the targets. Ages for NGC 2232 are estimated in Section 4 and Section 5 using the LDB method and fits to low-mass model isochrones, respectively. A comparison of these semi-independently derived ages and the implications for early stellar evolution and the cluster age-scale are discussed in Section 6.

2 TARGET SELECTION

2.1 NGC 2232

NGC 2232 is a bright, young open cluster located in Monoceros. It was first catalogued by Herschel (1864) and Dreyer (1888) and its distance first estimated by Collinder (1931; $d = 425$ pc). A spectroscopic study of 16 members by Levato & Malaroda (1974) reported $E(B - V) = 0.06 \pm 0.03$ mag and placed the cluster at 375 pc. Photometric studies by Claria (1972) and subsequently by Lyra et al. (2006) reported similar distance ($d = 360$ and 320 ± 30 pc, respectively), reddening [$E(B - V) = 0.01$ and 0.07 ± 0.02 mag] and ‘nuclear’ (main sequence turn-off) ages ($=20$ and 32 ± 15 Myr). Lyra et al. also reported an isochronal age of 25–32 Myr for low-mass PMS members.

A chemical abundance analysis of NGC 2232 F- and G-type stars by Monroe & Pilachowski (2010) found a super-solar metallicity of $[\text{Fe}/\text{H}] = 0.27 \pm 0.08$ dex and that their (probably still undepleted) Li-abundances were consistent with clusters of ~ 100 Myr or younger. No previous study has focused on Li-depletion in the lower mass stars of NGC 2232. There are 14 NGC 2232 targets (see Section 2.2) with spectral-types FGK that were observed in GES and that have high signal-to-noise ratio (SNR) spectra with reported $[\text{Fe}/\text{H}]$ values and uncertainties (see Appendix A). These metallicities were derived using the same methods as for other young clusters observed in GES (e.g. Spina et al. 2017) and have been externally verified against Gaia benchmark stars (Jofré et al. 2014). Based on these measurements, Appendix A suggests a near-solar metallicity for NGC 2232 of $[\text{Fe}/\text{H}] = 0.00$ with a dispersion of just 0.05 dex.

2.2 Selecting NGC 2232 members

NGC 2232 was observed as part of GES between 2015 November 6 and 11. Targets were selected in CMDs, based on their available optical and near-infrared (near-IR) photometry, from a broad region more than encompassing the likely location of cluster members. The spectra were recorded with the FLAMES fibre instrument (Pasquini et al. 2002), on ESO’s UT-2 Very Large Telescope, either with the UVES spectrograph (resolving power, $R \simeq 47\,000$, wavelength range $\lambda\lambda 4200 - 11000$ Å) for the minority of bright targets, or with the GIRAFFE intermediate resolution spectrograph

($R \sim 12\,000$, $\lambda\lambda 3700 - 9000 \text{ \AA}$). Both setups include the Li I 6708 \AA absorption line. Raw images were homogeneously analysed and spectra extracted and calibrated using standard GES pipelines (see Jeffries et al. 2014; Sacco et al. 2014; Randich et al. 2018). The spectra in this paper are from the fifth internal data release (GESiDR5¹).

A list of high probability members of NGC 2232 with GES spectroscopy was taken from Jackson et al. (2020). This study assigns membership using astrometry from Gaia DR2 (Gaia Collaboration 2018) and radial velocity (RV) measurements from GESiDR5. Since the membership probabilities are calculated using kinematics alone, the target list is unbiased with respect to the presence of lithium or indeed any age-related property. Of the 760 targets with spectroscopy, 80 have a membership probability $P_{3D} > 0.95$, with an average value of 0.992. Based on these probabilities we expect ≤ 1 contaminant in our list of members.

Since the publication of Jackson et al. (2020), the (early) Third Gaia Data Release has been made available (herein Gaia EDR3; Gaia Collaboration 2020). The statistical uncertainties for parallax measurements in Gaia EDR3 are typically ~ 30 per cent smaller and, more importantly, the systematic uncertainties due to possible correlated errors in the parallax zero-point on small spatial scales (Lindegren et al. 2018) have been significantly improved (Lindegren et al. 2020). Although the membership probabilities use Gaia DR2 astrometry, we measure the weighted mean cluster parallax (π_c) and distance modulus (d_{mod}) using Gaia EDR3 parallaxes as follows: first an intrinsic dispersion of the cluster parallax is estimated, equal to the standard deviation of cluster members minus the RMS parallax uncertainty (subtracted in quadrature). This dispersion is added in quadrature with the parallax uncertainties from each target and used as a weight to give a mean $\pi_c = 3.1355 \pm 0.0106 \pm 0.0300 \text{ mas}$ and $d_{\text{mod}} = 7.518 \pm 0.007 \pm 0.021 \text{ mag}$, where the two error bars represent the statistical error in the mean and a remaining systematic uncertainty [see Fig. 2(a) in Lindegren et al. 2020], respectively. The corresponding distance of $d = 319 \pm 1 \pm 3 \text{ pc}$ is very similar to Lyra et al. (2006) but with a much smaller error bar. We discuss how the distance measurement affects our analyses in Section 4 and Section 5.

We use Gaia DR2 G -band (optical) and K_s -band (near-IR) photometry for our analyses. This is because Gaia provides homogeneous G magnitudes with mmag-precision for all targets in our sample (our faintest target has $G \sim 19$) and absolute K_s magnitudes are preferable in identifying the LDB since they are highly sensitive to the peak flux from low-mass stars. Near-IR photometry is from 2MASS (Cutri et al. 2003) and the sixth data release of the Vista Hemisphere Survey (VHS; McMahon et al. 2019). There are 2MASS measurements available for all stars, and all these have the best possible flags for quality, contamination, and confusion (in all three bands). K_s magnitudes are also available for every target in VHS but bright targets have saturated at K_s . For 49 sources where the 2MASS $K_s < 13$ then that value is used. For 31 fainter sources, the VHS K_s photometry is adopted.

The $G - K_s$ colours are dereddened using the $E(B - V)$ value calculated in Lyra et al. (2006), $R_V = 3.09$, and $A_{K_s}/A_V = 0.114$ (Cardelli, Clayton & Mathis 1989), where A_G is estimated using the following fit to the A_G versus $G - K_s$ relation for main sequence stars provided in Danielski et al. (2018; see their Fig. 5, top middle

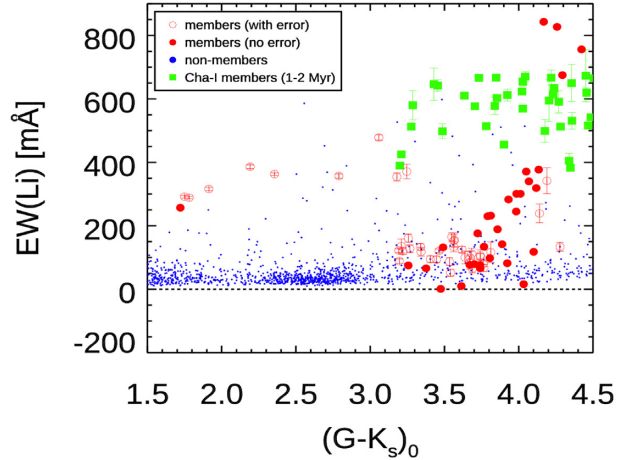


Figure 1. EW(Li) versus $(G - K_s)_0$ in NGC 2232, using EW(Li) measurements from GESiDR5. Red symbols represent the 80 high probability members ($P_{3D} > 0.95$). Open and filled symbols denote EW(Li) values with and without reported uncertainties in GESiDR5, respectively. Blue points are likely non-members of NGC 2232 ($P_{3D} < 0.1$) observed in the same instrument configurations as the members. The green squares are members of the ~ 2 Myr Cha I association also observed as part of GES.

panel),

$$A_G = A_V \times \frac{0.84 - 0.04(G - K_s) + A_{K_s}}{(1.0 - 0.04A_V)} \quad (1)$$

3 LITHIUM EQUIVALENT WIDTHS

3.1 GESiDR5

The equivalent width of the Li I 6708 \AA feature, EW(Li), is reported as part of the standard GESiDR5 analysis for all but two targets in our list. The method of measurement is described in Bouvier et al. (2016) and Randich et al. (2018).

The morphology of Fig. 1 suggests we are seeing the transition from Li-depleted stars at $(G - K_s)_0 < 4.0$ to Li-rich stars at $(G - K_s)_0 > 4.1$ that marks the LDB. The Li-rich stars have EW(Li) values comparable to those seen in $P_{3D} > 0.9$ members of the Cha I association (also taken from GESiDR5). Since Cha I has an age of only ~ 2 Myr (Luhman 2007) then this level of Li likely represents the undepleted local cosmic value.

Whilst these initial indications are promising, there are features in the plot that are at odds with expectations for the EW(Li)/colour distribution of a young open cluster. Firstly, stars immediately hotter than the LDB should be almost completely depleted of Li and their EW(Li) values should be ~ 0 . However, there appears to be a plateau, with mean EW(Li) $\simeq 120 \text{ m\AA}$, that is also present. This may be indicative of a systematic offset resulting from the EW estimation process in GESiDR5, which is supported by the fact that the EW(Li) of cluster non-members, which are almost certainly depleted of Li, also have EW(Li) > 0 . The process of measuring EW(Li) is complicated in M-dwarfs by molecular absorption features (e.g. Rajpurohit et al. 2014) and the pseudo-continuum is highly sensitive to small temperature changes. Errors in continuum placement can easily lead to systematic shifts in EW(Li), particularly in low SNR spectra. Secondly, most of the targets with $(G - K_s)_0 > 3.7$ do not have a reported error bar in GESiDR5. Given the SNR for these objects is low ($\lesssim 10$; see Fig. 3), it is important to quantify the EW(Li) uncertainties to determine whether the targets with large EW(Li) values are real detections

¹The GESiDR5 catalogue is available to the GES consortium at <http://ges.royalobservatory.ac.uk/>.

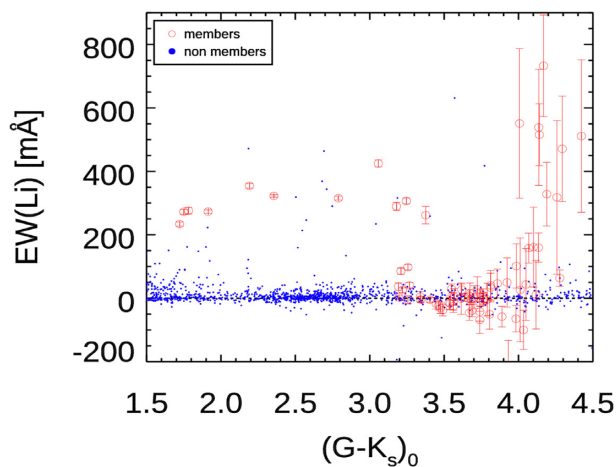


Figure 2. EW(Li) versus $(G - K_s)_0$, using the revised EW(Li) values (and errors) calculated from our analysis in Section 3.2. The symbols and notation are the same as those described in Fig. 1.

or simply cases of noisy data or uncertain pseudo-continuum placement.

3.2 Remeasuring EW(Li)

To address the issues identified with the GESiDR5 measurements, we independently measured EW(Li) using the reduced GESiDR5 spectra and a novel technique that is detailed in Appendix B. In brief, template Li-free spectra for a given $(G - K_s)_0$ colour were generated over the 6675–6730 Å range by making use of the large number of field stars serendipitously observed in the fields of GES clusters (i.e. those with kinematic cluster membership probabilities $P_{3D} < 0.1$). For M-dwarfs we can safely assume that the vast majority of these stars have no lithium at all. This is an entirely empirical approach to determining a continuum for cool stars and not reliant on the fidelity of model atmospheres. The FWHM of any Li feature is determined by the instrumental resolution and the rotational velocity of the star given by the VROT parameter in GESiDR5. EW(Li) is then estimated by comparing the target spectrum with the template that best matches its intrinsic colour and integrating over a Gaussian profile that characterizes the FWHM. Uncertainties are calculated by repeating this procedure for regions in the vicinity of the Li feature.

For some stars with low SNR there are no VROT values reported in GESiDR5. In these cases we assumed a value of 32 km s^{-1} , which is the mean value for the cluster M-dwarfs with VROT. Whilst the FWHM for these stars may be incorrect, the effects on the estimated EW(Li) are smaller than the error bars due to spectral noise and continuum placement. A visual inspection confirmed that the template continua appear well matched to the observations in all cases.

The EW(Li) versus $(G - K_s)_0$ plot for these new EW(Li) estimates is provided in Fig. 2 and in Fig. 3 we present the spectra for all NGC 2232 members with $(G - K_s)_0 > 3.8$. The issues highlighted in Section 3.1 appear to be resolved with our methods. The median EW(Li) value of targets in the Li-chasm ($3.3 < (G - K_s)_0 < 4.0$) is $-5 \pm 72 \text{ mÅ}$, as expected for stars that have no Li. Secondly, our analysis provides uncertainties for all targets, regardless of their SNR.

4 THE LDB OF NGC 2232

This section describes how the LDB is located in NGC 2232 (Section 4.1), the evolutionary models used in this work (Section 4.2), and the method to calculate an LDB age (Section 4.3). All data used in this work: P_{3D} , photometry, and EW(Li) values from both GESiDR5 (Section 3.1), and our own analysis (Section 3.2) are provided in Table C1.

4.1 Identifying the LDB location

Curve of growth models predict that a 99 per cent Li-depleted early/mid M-type star has an $\text{EW(Li)} \approx 300 \text{ mÅ}$ (Palla et al. 2007), compared with 600–700 mÅ for no depletion. Therefore we use $\text{EW(Li)} = 300 \text{ mÅ}$ to discriminate between Li-rich and Li-poor stars. Figs 4 shows the intrinsic $(G - K_s)_0/M_K$ CMD for the NGC 2232 members. Symbols are colour coded for whether EW(Li) is bigger or smaller than 300 mÅ. Objects that have EW(Li) within one error bar of this threshold are shown as open symbols and triangles indicate objects, which by virtue of their position in the CMD, are likely to be unresolved binaries (the exact criterion is discussed in Section 5).

The CMD show a reasonably clear boundary between Li-rich and Li-poor targets. There are few targets near the EW(Li) threshold, as expected, since the depletion of Li is rapid once it begins. Looking just at the ‘single star’ sequence we put the LDB somewhere in the grey, rectangular region separating Li-poor from Li-rich stars. The upper bound is defined by the faintest clear Li-poor star, the lower bound is defined by the brightest clear Li-rich star that lies redward of the Li-poor marker. The box width is defined by their separation in colour. Whilst this latter choice is somewhat arbitrary, changing the box width by factors of two does not significantly affect the calculated ages (see Section 4.3). There are two Li-rich stars that are more luminous than the defined LDB box, but these are most likely to be unresolved binaries that are displaced upwards by up to 0.75 mag in the CMD.

4.2 Evolutionary models

The evolutionary models adopted in this work are categorized as either ‘standard models’ or ‘magnetic models’. Standard models feature only convective mixing and do not take any account of the influence of magnetic activity on stellar structure. There are numerous standard models that differ in their input physics regarding the equation of state, treatment of convection, interior opacities, and atmospheres. As representatives of these, we consider the models of Dotter et al. (2008, herein, D08), Baraffe et al. (2015, herein, B15), and the spot-free models of Somers, Cao & Pinsonneault (2020, herein, S20).

Magnetic models incorporate some aspects of the dynamo-generated magnetism that is known to be present in these young, fast-rotating, magnetically active stars (Reiners & Basri 2009). Two evolutionary codes are considered: (i) The S20 models that incorporate the blocking of flux by dark, magnetic starspots at the stellar photosphere. These are available in increments of spot-coverage fractions (f_{sp}) of 0.17. The spots are taken to be at a temperature that is 80 per cent of the unspotted photosphere, meaning that about $0.59f_p$ of the radiative flux from the star is blocked by the starspots. The spot-free version is used as a standard model. (ii) The ‘magnetic Dartmouth models’ described in Feiden & Chaboyer (2014) and Feiden (2016, herein F16) that implement magnetic inhibition of convection constrained by a boundary condition of an average 2.5



Figure 3. GES spectra for the 24 targets with $(G - K_s)_0 > 3.8$. The normalized, reduced spectra from GESiDR5 are displayed in grey, where the data have been binned by 7 pixels. The best-matching spectral template (described in Section 3.2) is shown in the region encompassing the Li-feature at 6708 Å (in red) and in two regions either side of the feature (in blue). The title of each panel gives the Gaia DR2 source identifier, the SNR given in GESiDR5 and the $(G - K_s)_0$ colour. The EW(Li) values are provided in the bottom left of each panel, where targets defined as Li-rich are highlighted in larger red text.

kG magnetic field at the stellar surface and that is approximately the equipartition value at the surface of a mid-M dwarf. These models are approximately an extension of the D08 standard model.

For consistency, the $(G - K_s)_0$ and M_{K_s} values from each model are calculated from $\log T_{\text{eff}}$ and $\log L$, using the same, age-dependent

cubic relationships between colours and temperatures and between bolometric corrections and luminosities, derived from the models of Baraffe et al. (2015). Specific relationships were calculated at each age between 1.0 and 250.0 Myr (in steps of 0.1 Myr). This was done to remove any disparities due to the adoption of different

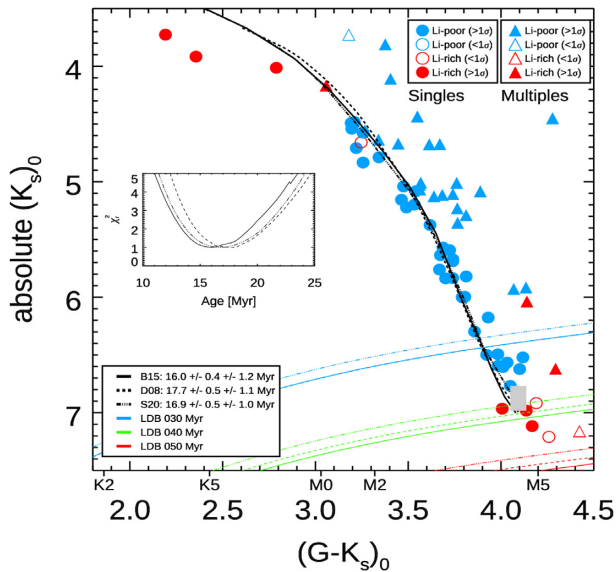


Figure 4. M_{K_s} versus $(G - K_s)_0$ for high probability cluster members. Red and blue symbols denote targets classed as Li-rich and Li-poor (in Section 4.1), where open and closed symbols denote whether the EW(Li) is within, or not within, one error bar of 300 mÅ. Circles and triangles represent the likely-single and likely-multiple stars (in Section 5), respectively. The grey box denotes the estimated position of the LDB. The blue, green, and red lines represent curves of constant luminosity at 99 per cent Li depletion from three standard models (see Section 4.2 for details) at 30, 40, and 50 Myr, respectively. The black curves are the best-fitting M_{K_s} versus $(G - K_s)_0$ isochrones to the likely single stars for the same models. The inset plot shows the reduced χ_r^2 as a function of isochrone age.

bolometric corrections in the native colour and magnitude predictions of each model. For the S20 models there is the added complexity in accounting for two photospheric temperatures: one from the cooler star-spot regions and another from the warmer surrounding photosphere. The G and K_s bolometric corrections in this case were calculated using equation (6) in Jackson & Jeffries (2014b), where the temperature ratio between the spotted surface and the photosphere was fixed at 0.8.

4.3 Estimating the LDB age of NGC 2232

Bolometric luminosities and ages at 99 per cent Li-depletion were interpolated from the mass tracks of each model. The age sampling from the models was fine enough to follow the rapid Li-burning phase in fully convective stars. Figs 4 and 5 show example loci of the luminosity at 99 per cent Li-depletion at ages of 30, 40, and 50 Myr that encompass the observed LDB location (grey box). The loci are curved because the bolometric corrections are colour dependent.

The LDB age is estimated as that of the 99 per cent depletion locus that passes through the centre of the LDB location. Age uncertainties are separated into a statistical and systematic component in Table 1. The statistical error bar is the quadrature sum due to the dimensions of the box defining the LDB location and corners the mean measurement error in $(G - K_s)_0$ and M_{K_s} of the two targets that sit either side of the box. The systematic error is calculated as the quadrature sum due to shifting the LDB box (together with all the data points) by the uncertainties in distance and reddening/extinction. A shift of 0.1 mag in the absolute magnitude of the LDB box corresponds to a shift in age of ~ 1 Myr. Horizontal shifts in the colour of the LDB are less important because the LDB luminosity loci are nearly horizontal.

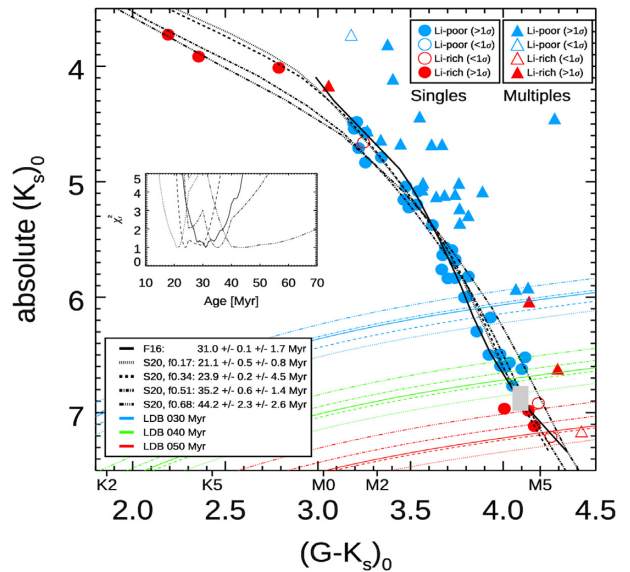


Figure 5. Similar to Fig. 4 but showing the loci of constant luminosity for 99 per cent Li depletion (coloured lines), the best-fitting isochrones (black lines) and χ_r^2 versus age for a series of magnetic models (see Section 4.2).

The overall age uncertainty is dominated by the vertical extent of the LDB box that contributes ~ 80 per cent of the error budget. We return to the effects of statistical and systematic errors on the LDB age in Section 6.

The LDB ages determined using the three standard models are shown in Table 1 and are in close agreement (36.9–39.0 Myr). The choice of standard model contributes about the same uncertainty (~ 5 per cent) as the total experimental uncertainties. This is unsurprising given that the physics in the interiors of fully convective stars is relatively well understood and the known insensitivity of the LDB to the physical differences in models (Burke et al. 2004; Tognelli et al. 2015). The analysis was repeated using the absolute $(G - J)_0/M_J$ diagram and the results are practically identical (see Table 1).

The magnetic models predict slightly older ages, by ~ 5 –20 per cent compared with their standard model counterparts. The S20 models indicate that increasing magnetic activity (or at least a larger f_{sp}) leads to older LDB ages. The results for the F16 model are similar to the S20 $f_{sp} = 0.34$ model. Again, the results using the $(G - J)_0/M_J$ diagram are almost identical.

There are enough data points surrounding the LDB box in Figs 4 and 5 that we are reasonably confident the results are robust. In summary, the LDB ages determined from standard models are 37–39 Myr and from magnetic models are 41–50 Myr, and higher spot coverage/magnetic activity leads to the older ages.

5 ISOCHRONAL AGES

Ages have also been estimated by fitting isochrones to the low-mass stars in absolute CMDs. Comparison is made in the observational plane since it makes the role of measurement uncertainties and systematic errors clear. Although a single d_{mod} value was adopted, cluster members will be at slightly different distances. The angular extent of the cluster members translates to a diameter of ~ 6 pc. A similar front-to-back depth is too small to be resolved by the EDR3 parallaxes, so will introduce a modest additional scatter of $\sim \pm 0.2$ mag to the absolute magnitudes of individual stars.

Table 1. Ages (in Myr) derived from the LDB method (Section 4) and from fitting isochrones to the CMD (Section 5). The first and second error bar are representative of the statistical and systematic uncertainties, respectively. For the CMD ages, the subsequent values are the number of targets that are used in the fitting process (N) and the figure-of-merit for the fit (ξ , described in Section 5), respectively. The upper section shows the results for standard models, the lower for magnetic models (see Section 4.2); B15 = Baraffe et al. (2015); D08 = Dotter et al. (2008); F16 = Feiden (2016); S20 = Somers et al. (2020). No sensible fit to the CMD could be obtained for the S20 f0.85 model.

Model	$(G - K_s)_{\text{LDB}}$	$(G - J)_{\text{LDB}}$	$(G - K_s)_{\text{CMD}}$	$(G - J)_{\text{CMD}}$
Standard models				
B15	$36.9 \pm 1.8 \pm 0.7$	$37.2 \pm 1.8 \pm 0.7$	$16.0 \pm 0.4 \pm 1.2, 37, 0.039$	$15.2 \pm 0.5 \pm 0.9, 34, 0.038$
D08	$37.5 \pm 1.9 \pm 0.8$	$37.8 \pm 2.0 \pm 0.8$	$17.7 \pm 0.5 \pm 1.1, 35, 0.034$	$16.1 \pm 0.6 \pm 1.2, 32, 0.039$
S20 (no spots)	$39.0 \pm 2.0 \pm 0.8$	$39.3 \pm 2.1 \pm 0.9$	$16.9 \pm 0.5 \pm 1.0, 43, 0.036$	$15.6 \pm 0.7 \pm 1.1, 42, 0.053$
Non-standard models				
F16	$43.2 \pm 2.1 \pm 0.8$	$43.5 \pm 2.2 \pm 0.9$	$31.0 \pm 0.1 \pm 1.7, 42, 0.033$	$31.0 \pm 0.9 \pm 1.1, 38, 0.044$
S20, f0.17	$40.8 \pm 2.0 \pm 0.8$	$41.0 \pm 2.1 \pm 0.9$	$21.1 \pm 0.5 \pm 0.8, 42, 0.023$	$20.7 \pm 0.2 \pm 0.6, 40, 0.037$
S20, f0.34	$42.7 \pm 2.1 \pm 0.9$	$43.0 \pm 2.2 \pm 0.9$	$23.9 \pm 0.2 \pm 4.5, 43, 0.026$	$23.5 \pm 0.2 \pm 3.5, 40, 0.041$
S20, f0.51	$44.8 \pm 2.2 \pm 0.9$	$45.1 \pm 2.3 \pm 1.0$	$35.2 \pm 0.6 \pm 1.4, 43, 0.024$	$34.0 \pm 0.4 \pm 1.2, 42, 0.041$
S20, f0.68	$47.3 \pm 2.5 \pm 1.0$	$47.7 \pm 2.6 \pm 1.0$	$44.2 \pm 2.3 \pm 2.6, 43, 0.052$	$44.5 \pm 1.6 \pm 2.7, 42, 0.056$
S20, f0.85	$50.6 \pm 2.7 \pm 1.1$	$50.2 \pm 2.7 \pm 1.1$	–	–

Cluster members will include a fraction of multiple systems that are brighter than single stars of the same colour. Including these in the isochrone fitting would bias the fits towards younger ages. Therefore we define a faint subsample that are likely to be single stars. These are cluster members with M_{K_s} greater than the interpolated value calculated from a second-order polynomial fit to M_{K_s} versus $(G - K_s)_0$ for the full target sample. Finally, we only retain targets for fitting that have $(G - K_s)_0 > 1.9$, since hotter and more luminous stars are likely to have reached the main sequence and will simply add noise to the fit. This leaves 43 ‘faint’ members, likely to be single stars that are denoted by circles in Figs 4 and 5 and 28 ‘bright’ members (triangles), which are likely binary (or higher order multiple) systems. The spectral-types corresponding to the $(G - K_s)_0$ axes are from the main-sequence interpolation table provided by E. Mamajek.²

To estimate isochronal ages, a fit to the single stars is made using the same model isochrones and bolometric corrections described in Section 4.2 at fixed values of d_{mod} and $E(B - V)$. The best-fitting age minimizes $\Delta^2/(N - 1)$, where Δ^2 is the sum of the squared residuals in M_{K_s} between the data and model isochrones, and N is the number of targets within the colour range covered by the model isochrone.

This quantity provides a figure-of-merit that can be compared across different models. This method assumes that individual M_{K_s} uncertainties are homoscedastic and accounts for the fact that the dispersion around the best fit is large compared with the formal uncertainties in M_{K_s} from the photometry and adopted uniform distance – probably because of stellar variability, rotational modulation and flares, the presence of some unresolved low mass-ratio binaries, and perhaps as a result of varying spot coverage. The minimum value of $\Delta^2/(N - 1)$ for each model is reported in Table 1 along with the best-fitting isochrone.

To estimate statistical uncertainties in the ages, $\Delta^2/(N - 1)$ is converted to a χ^2 -like statistic by normalizing the Δ^2 values so that the best-fitting $\Delta^2_{\text{min}}/(N - 1) = 1$. Uncertainties are then estimated from the ages at which the normalized $\Delta^2 = N$. This is equivalent to finding the ages such that $\chi^2 = (N - 1)\chi^2_{r,\text{min}} + 1$. The statistical age uncertainties are small (≤ 0.6 Myr for all fits except the spottiest model).

²https://www.pas.rochester.edu/~emamajek/EEM_dwarf_UBVIJHK_color_s_Teff.txt

Systematic age uncertainties arise from the assumed values of $d_{\text{mod}} = 7.518 \pm 0.021$ and $E(B - V) = 0.07 \pm 0.02$. A larger distance and smaller reddening lead to younger ages. Since uncertainties in d_{mod} (from parallax) and $E(B - V)$ should be uncorrelated, then an additional systematic uncertainty was estimated from the quadrature sum of offsets in fitted age caused by changing d_{mod} and $E(B - V)$ (and the extinction) by their error bars. The best-fitting ages with both statistical and systematic error bars are reported in Table 1.

5.1 Standard models

Fig. 4 shows the M_{K_s} versus $(G - K_s)_0$ CMD, with the best-fitting isochrones from the three standard models. The best-fitting ages are given in the upper part of Table 1. The estimated ages are in close agreement; the age range of 16.0–17.7 Myr is comparable to the error bars. Ages from the M_J versus $(G - J)_0$ are about 1 Myr younger.

The standard models appear to be poor fits overall. They are all systematically overluminous by 0.1 – 0.4 mag at the hot end of the data set and underluminous by ~ 0.2 mag at the lowest temperatures.

In contrast to the LDB ages, many stars are used in the fits to define an isochronal age and therefore the statistical precision of the ages is comparable to or better than the systematic errors attributable to distance and reddening uncertainty. An additional systematic uncertainty in the case of the isochrone fitting is the cut that was applied to define binary stars that were excluded from the fit. The default cut excluded 39 percent of the members as binaries. The binary fraction among low-mass stars is unlikely to be larger than this and could well be smaller. We tested the impact of this by offsetting the threshold curve in the CMD that defined binarity until only 25 percent of stars were considered binaries. The resulting isochronal fits were younger by just 1 Myr and so we do not consider this any further as a significant source of age uncertainty.

5.2 Magnetic models

Fig. 5 shows the results of fitting the magnetic model isochrones to the same data. The results are given in the lower part of Table 1. Two features are immediately clear: the magnetic models predict much older isochronal ages and a larger spread in age (from 21 to 44 Myr) than the standard models. The spread is due to the range of magnetic activity considered. The youngest ages are for the least-spotted S20 models and the oldest are for the most-spotted models.

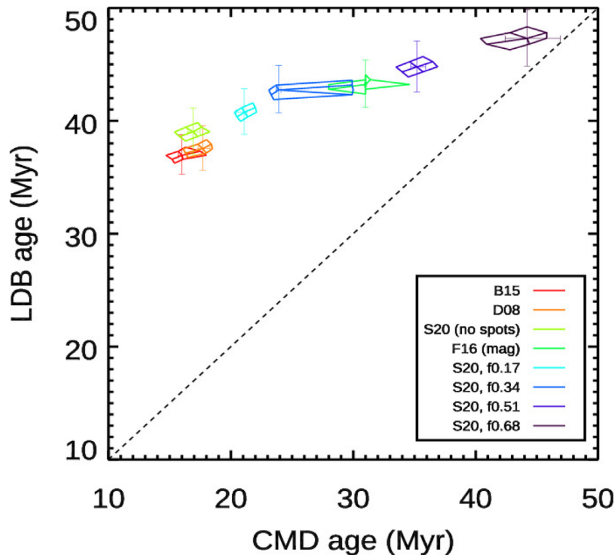


Figure 6. A comparison of the LDB- and CMD-derived ages from each model. Vertical and horizontal error bars represent the age error due to statistical uncertainty and the grids demonstrate the effect on the derived age when altering $E(B - V)$ and d_{mod} by their error bars (representing systematic uncertainties). The dotted line denotes equivalence.

The F16 magnetic models yield an age somewhere between the $f_{\text{sp}} = 0.34$ and $f_{\text{sp}} = 0.51$ models of S20. The χ^2 landscape of the fits to the magnetic models is more complex than for the standard models and in some cases results in larger uncertainties, both statistical and systematic (particularly for the $f_{\text{sp}} = 0.34$ model).

The average absolute gradient of the S20 models become smaller with increasing f_{sp} . The net effect of increasing the star-spot coverage in cooler stars is to cause inflated radii, lower T_{eff} , and a higher luminosity at a given age. For higher-mass stars, with radiative cores, the radius inflation is much less and the luminosity is reduced. The S20 models with $0.17 \leq f_{\text{sp}} \leq 0.51$ provide the best fits to the data according to the unnormalized $\Delta^2/(N - 1)$ statistic and they appear to fit the data better than any of the standard models. The significance of this can be assessed using the difference in $\text{Mln } \Delta^2$, equivalent to the Akaike information criterion in least squares fitting. For example, this difference is 17.44 between the $f_{\text{sp}} = 0.51$ and the equivalent unspotted S20 models; a likelihood ratio of $\exp(-17.44/2) = 1.6 \times 10^{-4}$ in favour of the spotted model.

A more spotted $f_{\text{sp}} = 0.68$ model, however, provides a significantly worse fit. It matches the high-mass stars reasonably, but becomes increasingly overluminous redward of $(G - K_s) = 3.5$. We were unable to find any reasonable fit for a $f_{\text{sp}} = 0.85$ model and discarded these from our analysis. The F16 models provide a reasonable fit at low masses, but they do not extend to colours blueward of $(G - K_s) = 3.0$ where they appear overluminous by ~ 0.2 mag.

6 DISCUSSION

Fig. 6 compares the ages estimated from the LDB and CMD method for each model. The errors due to statistical and systematic uncertainty are indicated. Statistical errors dominate for the LDB ages because the LDB location is determined by only a handful of stars. The effects of systematic errors due to uncertainties in distance and reddening are small. In contrast, many more data points define the best-fitting CMD ages and the effects of distance and reddening uncertainties are comparable or larger than the statistical errors.

The LDB ages are older than the CMD ages for all the models tested; much older (by factors of ≥ 2) for standard models, but becoming closer, but with older ages, for models featuring increasing levels of magnetic activity, to the extent that there is marginal consistency for the $f_{\text{sp}} = 0.68$ model of S20. There is excellent internal agreement between the standard models in terms of what they give for the LDB ages, the CMD ages, and their ratio, despite the differing ingredients in these models in terms of atmospheres, convection, and boundary conditions. There are much larger differences between the magnetic models, but that is expected since they represent differing levels of magnetic activity. What is notable about Fig. 6 is how little the LDB ages increase with increased magnetic activity compared to the very large increases in CMD age. In other words, the LDB ages are *much* less sensitive to the effects of magnetic activity, and even less so to other varying model inputs (see also Burke et al. 2004; Jackson & Jeffries 2014b; Tognelli et al. 2015), and should therefore be given more weight.

That the magnetic models predict CMD ages for NGC 2232 up to 2–3 times older than from standard models is in broad agreement with Bell et al. (2013), who found that low-mass isochronal ages needed to be significantly increased to match ages found from isochronal fits to high-mass members of the same young clusters. It also agrees with work that finds the isochronal ages and the ages inferred from the general pattern of Li-depletion among low-mass members of young clusters do not agree when using standard models, but might be brought into agreement at significantly older ages if the low-mass stars are inflated by magnetic activity and starspots (Somers & Pinsonneault 2015; Jeffries et al. 2017). The turn-off age of NGC 2232 is rather uncertain and based on few stars, 32 ± 15 Myr using models with some core overshooting (Lyra et al. 2006), and might agree with any of the ages in this work.

It appears that very high levels of magnetic activity or spot coverage ($f_{\text{sp}} \geq 0.68$) might be required, in order to bring isochronal and LDB ages into agreement at ≥ 45 Myr, although the very high spot coverage models are not a good fit to the entire low-mass sequence in NGC 2232. There is however no compelling reason why spot coverage or magnetic activity should be uniform with stellar mass. It could be that the lower mass stars have much higher levels of spot coverage, for example. A ‘hybrid model’, featuring higher spot coverage at lower masses, with fewer spots at higher masses or models with cooler spots could provide an excellent fit to the CMD. Zeeman Doppler Imaging studies do suggest that the magnetic field strength in the higher mass stars is weaker than in the low-mass stars [see e.g. fig. 10 in Folsom et al. (2018) and fig. 14 in Kochukhov (2021)].

Is a >50 percent spot covering fraction realistic for the low mass stars in NGC 2232? M-dwarf members of young clusters are generally found to be both rapidly rotating and highly magnetically active. The M-dwarfs in NGC 2547, which has a similar LDB age of 35 ± 3 Myr (based on standard models; Jeffries & Oliveira 2005) have saturated levels of coronal X-ray activity (Jeffries et al. 2011). It has been verified that highly-active M-dwarfs have strong magnetism, consistent with equipartition magnetic fields covering all of their surfaces (Reiners & Basri 2009; Morin et al. 2010). Jackson, Jeffries & Maxted (2009) find that a high spot coverage (>50 per cent) is needed to fit the CMD for M-dwarfs in NGC 2516 (age ~ 120 Myr); Fang et al. (2016) estimated f_{sp} values of up to 50 per cent for Pleiades K- and M-dwarfs at ~ 100 Myr by modelling their molecular absorption bands, and Jackson, Deliyannis & Jeffries (2018) found evidence that these M-dwarfs were correspondingly larger than predicted by standard evolutionary models and in better accord with the magnetic models.

7 SUMMARY

A combination of astrometry from the Gaia mission and EW(Li) observations from GES has been used to select a high probability set of low-mass members in NGC 2232. We have identified the LDB – the luminosity at which low mass stars switch from having undepleted photospheric Li to having no detectable Li at only slightly higher luminosities. The LDB is used to determine the age of the cluster with standard evolutionary models and also with ‘magnetic models’ that incorporate magnetic suppression of convection or the blocking of flux by dark, magnetic starspots at the surface. These ages are compared with those determined by fitting isochrones to low-mass stars in CMDs using the same models. The results and conclusions are as follows:

(i) The LDB age of NGC 2232 is 38 ± 3 Myr using standard models. The uncertainty is dominated by locating the LDB, which is defined by only a few stars. Systematic errors due to the adopted distance and reddening, or choice of standard model, are less important.

(ii) LDB ages using the magnetic models are between 41 and 50 Myr, with similar error bars. The inferred age increases with the fraction of the stellar photospheres assumed to be covered with dark spots.

(iii) Isochronal ages from fitting the CMD are more than a factor of two younger (15–18 Myr) than the LDB ages in the case of the standard models, but can be much closer (20–44 Myr) for magnetic models, with agreement between the separate techniques being best for models with spot coverage fractions >50 per cent.

The LDB ages are much more robust to the input physics and the levels of magnetic activity assumed. The strong disagreement between the LDB ages and ages derived from isochrone fits using the standard models indicates that there is missing physics in those models. The much better agreement between the LDB and isochronal ages for the magnetic models suggests that these offer a significantly better description of the early evolution of low-mass stars. If so, then ages determined by fitting isochrones to young, low-mass stars using standard models will need to be revised upwards by factors of 2–3, and masses inferred from standard models and the positions of low-mass stars in the CMD or Hertzsprung–Russell diagram will be underestimates.

ACKNOWLEDGEMENTS

ASB, RDJ, and RJJ acknowledge the financial support of the Science and Technology Facilities Council (STFC). We are grateful to I Baraffe for providing a version of the B15 models with finer age sampling that was used in our analysis of the lithium depletion boundary.

Based on data products from observations made with European Southern Observatory (ESO) Telescopes at the La Silla Paranal Observatory under programme ID 188.B-3002. These data products have been processed by the Cambridge Astronomy Survey Unit (CASU) at the Institute of Astronomy, University of Cambridge, and by the FLAMES/UVES reduction team at Istituto Nazionale di Astrofisica (INAF)/Osservatorio Astrofisico di Arcetri. These data have been obtained from the Gaia-ESO Survey Data Archive, prepared and hosted by the Wide Field Astronomy Unit, Institute for Astronomy, University of Edinburgh, which is funded by the UK Science and Technology Facilities Council. This work was partly supported by the European Union FP7 programme through European Research Council (ERC) grant number 320360 and by the Leverhulme Trust

through grant RPG-2012-541. We acknowledge the support from INAF and Ministero dell’ Istruzione, dell’ Università e della Ricerca (MIUR) in the form of the grant ‘Premiale VLT 2012’. The results presented here benefit from discussions held during the Gaia-ESO workshops and conferences supported by the ESF (European Science Foundation) through the GREAT Research Network Programme. This work has made use of data from the European Space Agency (ESA) mission Gaia (<https://www.cosmos.esa.int/gaia>), processed by the Gaia Data Processing and Analysis Consortium (DPAC, <https://www.cosmos.esa.int/web/gaia/dpac/consortium>). Funding for the DPAC has been provided by national institutions, in particular the institutions participating in the Gaia Multilateral Agreement.

8 DATA AVAILABILITY STATEMENT

The quantities used to perform the analyses in Section 4 and Section 5 are presented in Table C1. All the data are available from the ESO archive in the form of raw and reduced spectra.³

REFERENCES

- Baraffe I., Homeier D., Allard F., Chabrier G., 2015, *A&A*, 577, A42
 Beccari G. et al., 2017, *A&A*, 604, A22
 Bell C. P. M., Naylor T., Mayne N. J., Jeffries R. D., Littlefair S. P., 2013, *MNRAS*, 434, 806
 Bildsten L., Brown E. F., Matzner C. D., Ushomirsky G., 1997, *ApJ*, 482, 442
 Binks A. S., Jeffries R. D., 2014, *MNRAS*, 438, L11
 Binks A. S., Jeffries R. D., 2016, *MNRAS*, 455, 3345
 Bouvier J. et al., 2016, *A&A*, 590, A78
 Bouvier J. et al., 2018, *A&A*, 613, A63
 Burke C. J., Pinsonneault M. H., Sills A., 2004, *ApJ*, 604, 272
 Cardelli J. A., Clayton G. C., Mathis J. S., 1989, *ApJ*, 345, 245
 Casali G. et al., 2019, *A&A*, 629, A62
 Casali G. et al., 2020, *A&A*, 639, A127
 Claria J. J., 1972, *A&A*, 19, 303
 Collinder P., 1931, *Ann. Obs. Lund*, 2, B1
 Cutri R. M. et al., 2003, *VizieR Online Data Catalog*, 2246,
 Damiani F. et al., 2014, *A&A*, 566, A50
 Danielski C., Babusiaux C., Ruiz-Dern L., Sartoretti P., Arenou F., 2018, *A&A*, 614, A19
 De Marchi G., Panagia N., Guarcello M. G., Bonito R., 2013, *MNRAS*, 435, 3058
 Dotter A., Chaboyer B., Jevremović D., Kostov V., Baron E., Ferguson J. W., 2008, *ApJS*, 178, 89
 Dreyer J. L. E., 1888, *Mem. R. Astron. Soc.*, 49, 1
 Fang X.-S., Zhao G., Zhao J.-K., Chen Y.-Q., Bharat Kumar Y., 2016, *MNRAS*, 463, 2494
 Feiden G. A., 2016, *A&A*, 593, A99
 Feiden G. A., Chaboyer B., 2013, *ApJ*, 779, 183
 Feiden G. A., Chaboyer B., 2014, *ApJ*, 789, 53
 Folsom C. P. et al., 2018, *MNRAS*, 474, 4956
 Gaia Collaboration, 2018, *A&A*, 616, A1
 Gaia Collaboration, Brown A. G. A., Vallenari A., Prusti T., de Bruijne J. H. J., Babusiaux C., Biermann M., 2020, *A&A*, 649, 20
 Gilmore G. et al., 2012, *Messenger*, 147, 25
 Gray D. F., 1984, *ApJ*, 277, 640
 Haisch K. E. Jr, Lada E. A., Lada C. J., 2001, *ApJ*, 553, L153
 Herczeg G. J., Hillenbrand L. A., 2015, *ApJ*, 808, 23
 Herschel J. F. W., 1864, *Phil. Trans. R. Soc.*, 154, 1
 Horne J. H., Baliunas S. L., 1986, *ApJ*, 302, 757
 Jackson R. J., Jeffries R. D., 2014a, *MNRAS*, 441, 2111

³<https://archive.eso.org/cms/eso-archive-news/New-data-release-DR4-from-the-Gaia-ESO-Spectroscopic-Public-Survey.html>

Jackson R. J., Jeffries R. D., 2014b, *MNRAS*, 445, 4306
 Jackson R. J., Jeffries R. D., Maxted P. F. L., 2009, *MNRAS*, 399, L89
 Jackson R. J. et al., 2015, *A&A*, 580, A75
 Jackson R. J., Deliyannis C. P., Jeffries R. D., 2018, *MNRAS*, 476, 3245
 Jackson R. J. et al., 2020, *MNRAS*, 496, 4701
 Jeffries R. D., Oliveira J. M., 2005, *MNRAS*, 358, 13
 Jeffries R. D., Littlefair S. P., Naylor T., Mayne N. J., 2011, *MNRAS*, 418, 1948
 Jeffries R. D., Naylor T., Mayne N. J., Bell C. P. M., Littlefair S. P., 2013, *MNRAS*, 434, 2438
 Jeffries R. D. et al., 2014, *A&A*, 563, A94
 Jeffries R. D. et al., 2017, *MNRAS*, 464, 1456
 Jofré P. et al., 2014, *A&A*, 564, A133
 Kochukhov O., 2021, *A&A Rev.*, 29, 1
 Kraus A. L., Cody A. M., Covey K. R., Rizzuto A. C., Mann A. W., Ireland M. J., 2015, *ApJ*, 807, 3
 Kraus A. L. et al., 2017, *ApJ*, 845, 72
 Levato H., Malaroda S., 1974, *AJ*, 79, 890
 Lindegren L. et al., 2018, *A&A*, 616, A2
 Lindegren L. et al., 2020, *A&A*, 649, 31
 Luhman K. L., 2007, *ApJS*, 173, 104
 Lyra W., Moitinho A., van der Bliek N. S., Alves J., 2006, *A&A*, 453, 101
 MacDonald J., Mullan D. J., 2017, *ApJ*, 834, 67
 MacDonald J., Mullan D. J., 2021, *ApJ*, 907, 27
 McMahon R. G. et al., 2019, *VizieR Online Data Catalog*, II, 359
 Malo L., Artigau É., Doyon R., Lafrenière D., Albert L., Gagné J., 2014a, *ApJ*, 788, 81
 Malo L. et al., 2014b, *ApJ*, 792, 37
 Mamajek E. E., Meyer M. R., Hinz P. M., Hoffmann W. F., Cohen M., Hora J. L., 2004, *ApJ*, 612, 496
 Manara C. F. et al., 2020, *A&A*, 639, A58
 Martín E. L., Lodieu N., Pavlenko Y., Béjar V. J. S., 2018, *ApJ*, 856, 40
 Monroe T. R., Pilachowski C. A., 2010, *AJ*, 140, 2109
 Morales J. C. et al., 2009, *ApJ*, 691, 1400
 Morin J., Donati J. F., Petit P., Delfosse X., Forveille T., Jardine M. M., 2010, *MNRAS*, 407, 2269
 Muzerolle J., Calvet N., Briceño C., Hartmann L., Hillenbrand L., 2000, *ApJ*, 535, L47
 Naylor T., 2009, *MNRAS*, 399, 432
 Palla F., Randich S., Pavlenko Y. V., Flaccomio E., Pallavicini R., 2007, *ApJ*, 659, L41
 Pasquini L. et al., 2002, *Messenger*, 110, 1
 Rajpurohit A. S., Reylé C., Allard F., Scholz R.-D., Homeier D., Schultheis M., Bayo A., 2014, *A&A*, 564, A90
 Randich S., Gilmore G., Gaia-ESO Consortium, 2013, *Messenger*, 154, 47
 Randich S. et al., 2018, *A&A*, 612, A99
 Reiners A., Basri G., 2009, *ApJ*, 705, 1416
 Rizzuto A. C., Dupuy T. J., Ireland M. J., Kraus A. L., 2020, *ApJ*, 889, 175
 Sacco G. G. et al., 2014, *A&A*, 565, A113
 Silverberg S. M. et al., 2020, *ApJ*, 890, 106
 Soderblom D. R., 2010, *ARA&A*, 48, 581
 Soderblom D. R., Hillenbrand L. A., Jeffries R. D., Mamajek E. E., Naylor T., 2013, in Beuther H., Klessen R. S., Dullemond C. P., Henning T., eds, *Protostars and Planets VI*, University of Arizona Press, Tucson
 Somers G., Pinsonneault M. H., 2015, *MNRAS*, 449, 4131
 Somers G., Cao L., Pinsonneault M. H., 2020, *ApJ*, 891, 29
 Spina L. et al., 2017, *A&A*, 601, A70
 Stauffer J. R., Schultz G., Kirkpatrick J. D., 1998, *ApJ*, 499, L199
 Stauffer J. R. et al., 1999, *ApJ*, 527, 219
 Tognelli E., Prada Moroni P. G., Degl'Innocenti S., 2015, *MNRAS*, 449, 3741
 Torres G., 2013, *Astron. Nachr.*, 334, 4

APPENDIX A: THE METALLICITY OF NGC 2232

There are 14 NGC 2232 members with [Fe/H] measured in GESiDR5 that have corresponding uncertainties and are therefore deemed reli-

Table A1. Metallicity values for the 14 NGC 2232 targets observed with the GIRAFFE spectrograph. The values in this table are those reported in the GESiDR5 catalogue. The final [Fe/H] value is the mean value, and the two error bars are the standard deviation and standard error in the mean, respectively.

GES Name (GES J-)	SNR	[Fe/H] dex	T_{eff} (K)
06283370 – 0446583	121	-0.094 ± 0.034	5797 ± 193
06250357 – 0456194	181	-0.083 ± 0.076	6316 ± 121
06262350 – 0416106	48	-0.035 ± 0.073	4243 ± 140
06293045 – 0441236	137	-0.034 ± 0.008	4934 ± 161
06281077 – 0432425	91	-0.033 ± 0.037	4503 ± 4
06284806 – 0442437	88	-0.006 ± 0.020	4988 ± 99
06274602 – 0446224	196	$+0.002 \pm 0.081$	5978 ± 52
06281883 – 0450578	52	$+0.004 \pm 0.163$	4046 ± 116
06274774 – 0440331	134	$+0.013 \pm 0.054$	5785 ± 123
06254936 – 0449006	76	$+0.020 \pm 0.092$	4760 ± 17
06285630 – 0449096	123	$+0.035 \pm 0.021$	5181 ± 198
06262866 – 0437367	153	$+0.068 \pm 0.002$	5970 ± 41
06262777 – 0433218	177	$+0.071 \pm 0.105$	6054 ± 245
06251933 – 0442048	135	$+0.077 \pm 0.023$	5468 ± 122
Final [Fe/H] = $0.000 \pm 0.054 \pm 0.014$ dex			

able measurements, all of which were obtained using the GIRAFFE spectrograph. These are listed in Table A1, where the T_{eff} indicate the majority of these stars are of F-K-type. Both the weighted mean [Fe/H] for these targets and the metallicity range across individual stars suggests the metallicity of NGC 2232 ([Fe/H] = 0.00 ± 0.014) is entirely consistent with a solar value, and similar to the metallicity of most nearby, young open clusters observed in GES (Spina et al. 2017). No evidence of a super-solar [Fe/H] is found, as reported by Monroe & Pilachowski (2010).

APPENDIX B: USING EMPIRICAL CONTINUUM SPECTRA TO ESTIMATE EW(LI) FOR K- AND M-DWARF STARS

This section describes the method used to estimate the EW(Li) of K- and M-dwarfs in NGC 2232 using the GESiDR5 spectra observed with the GIRAFFE spectrograph and 665 nm (HR15n) filter. The method proceeds in four steps.

B1 Sample selection

Jackson et al. (2020), hereafter J20, used GESiDR5 data to estimate membership probabilities for 10817 HR15n targets in 32 open clusters. Of these, 4390 were identified as likely cluster members with membership probability $P_{3D} > 0.9$ and 5726 as likely field stars with $P_{3D} < 0.1$ (see table 3 of J20). Spectra of these targets were analysed to determine their spectral indices using the procedure described in Damiani et al. (2014). In particular, the temperature-sensitive τ index was calculated to estimate $(G - K_s)_0$ for dwarf field stars of unknown reddening.

A subset of the data corresponding to likely dwarf cluster members with Gaia DR2 parallaxes > 1 mas was used to determine a fourth order polynomial relation of $(G - K_s)_0$ as a function τ over the range $1.85 < \tau < 2.8$ using the cluster reddenings shown in table 1 of J20. The polynomial fit, shown in Fig. B1, was then used to estimate $(G - K_s)_0$ values for the sample of likely field stars.

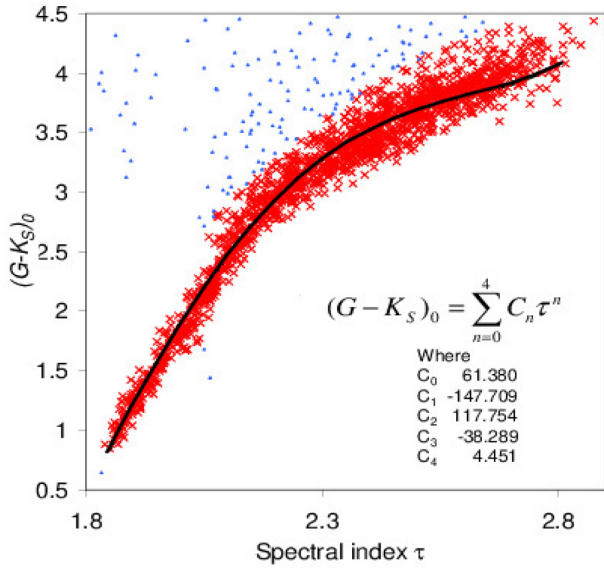


Figure B1. $(G - K_s)_0$ versus temperature index τ for $P_{3D} > 0.9$ cluster members with Gaia DR2 parallax $> 1''$ (see table 3 of J20). The black curve shows a polynomial fit to the measured data using coefficients shown on the plot. Red crosses are data used to fit the curve, blue triangles are outliers excluded from the fit.

B2 Empirical continuum spectra

A set of dwarf field stars were selected with good G and K_s photometry, a parallax > 1 mas and low levels of $\text{EW}(\text{Li})$ reported in GESiDR5 ($\text{EW}(\text{Li}) < 50$ mÅ for targets with $(G - K_s)_0 < 3.6$ and

$\text{EW}(\text{Li}) < 200$ mÅ for cooler stars). Targets were binned by $(G - K_s)_0$ colour in ± 0.1 mag wide bins in steps of 0.1 mag between $1.6 < (G - K_s)_0 < 4.0$.

The spectra were offset to their rest wavelength scale using the GESiDR5 RV and normalized to their median value over the wavelength range 6675–6730 Å. Empirical continuum spectra were calculated as the median of the normalized spectra in each bin at each point over the wavelength range. The uncertainty in the continuum spectrum was estimated as 1.3 times the median absolute deviation of the sample spectra relative to the median continuum spectrum.

Examples of continuum spectra and their associated uncertainties are shown in Fig. B2 for $1.6 < (G - K_s)_0 < 4.0$. The spectra of late M-dwarfs change considerably due to developing molecular absorption. Uncertainties in the continuum spectra increase from ~ 1 per cent for the warmest stars to ~ 7 per cent at $(G - K_s)_0 = 4$. These uncertainties were used to estimate the additional uncertainties in $\text{EW}(\text{Li})$ due to potential mismatch between the median continuum spectra and an ‘ideal’ continuum spectrum for a particular target.

It is recognized that some of the targets used to define these median spectra may not be fully Li-depleted. However, in M-dwarfs the depletion of Li takes place very rapidly and there should be few field M-dwarfs with low, but non-zero $\text{EW}(\text{Li})$. This is supported by the absence of any sign of a lithium feature in any of the median spectra.

B3 FWHM of target spectra in NGC 2232

An optimal extraction algorithm (Horne & Baliunas 1986) was used to measure $\text{EW}(\text{Li})$ where the FWHM of the extraction profile is a function of the spectral resolution and target $v \sin i$. The GES pipeline used to estimate rotational velocities for GESiDR5 data assumes a fixed spectral resolving power of $R \sim 17000$ for filter

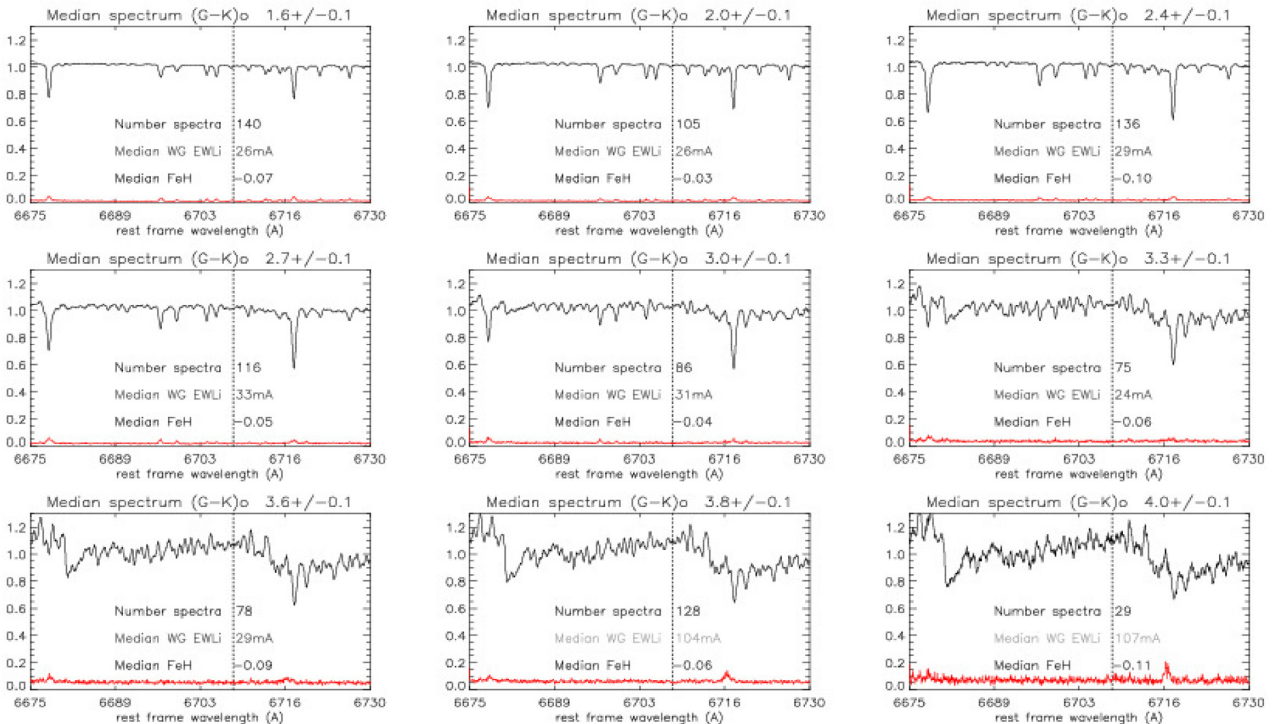


Figure B2. Examples of median continuum spectra for stars with low levels of Li as a function of $(G - K_s)_0$. Text on each plot shows the number of spectra averaged in each bin and median values of $\text{EW}(\text{Li})$ and $[\text{Fe}/\text{H}]$. The lower red curve shows the uncertainty in the continuum waveform, calculated as 1.3 times the median absolute deviation of individual spectra from the median spectrum. The dotted line indicates the position of the Li I 6708 Å absorption line.

HR15n. However, over the period when NGC 2232 was observed the resolution measured from the line width of daily arc-lamp spectra was unusually low, varying between $R = 12075$ and $R = 12534$ (J20). For this reason the GESiDR5 rotational velocities (VROT) were corrected to give a reduced value, $v \sin i$, as detailed in appendix A of J20. The FWHM of the extraction profile was calculated as

$$\text{FWHM} = \frac{\lambda_{\text{Li}}}{R} \left[1 + \frac{(v \sin i)^2}{C^2} \right];$$

where $C = \left[\frac{1 - u/3}{1 - 7u/15} \right]^{\frac{1}{2}} \frac{c}{R\sqrt{2 \ln 2}}$, (B1)

where λ_{Li} is the wavelength of the Li line at 6708 \AA and R is the resolving power on the day the target was observed. The term $(v \sin i)^2/C^2$ represents the effect of rotational broadening, taken from Gray (1984), for a star with limb darkening coefficient u (see Jackson et al. 2015, appendix A).

B4 measurement of EW(Li)

EW(Li) was measured by comparing target spectra (corrected to a rest wavelength scale) to the median continuum spectrum matched

to the target $(G - K_s)_0$ colour and scaled to match the continuum spectrum either side of the Li line over wavelength ranges, $6685\text{--}6705 \text{ \AA}$ and $6711\text{--}6717 \text{ \AA}$. A weighted profile $P(\lambda)$ was used to estimate EW(Li) from the difference between the target ($S_T(\lambda)$) and template ($S_C(\lambda)$) spectra,

$$\text{EW(Li)} = \int [S_C(\lambda) - S_T(\lambda)] P(\lambda) d\lambda / \int P(\lambda)^2 d\lambda, \quad (\text{B2})$$

where $P(\lambda)$ is a Gaussian profile with the predicted FWHM of the target spectrum. The uncertainty in EW(Li) was estimated as the RMS value of the EWs measured using the same procedure with $P(\lambda)$ centred at 15 offset wavelengths to the left of the Li line and 5 to the right. The systematic uncertainty in EW(Li) was estimated as a function of the Gaussian profile and the uncertainty spectrum at the appropriate $(G - K_s)_0$ colour. Results are shown in Table A1 and Fig. 2.

APPENDIX C: DATA FOR ALL NGC 2232 TARGETS

Table C1 presents the relevant data for all 80 stars that constitute our target sample.

Table C1. Gaia DR2 source identifiers (column 1), membership probabilities (P_{3D} , column 2), photometry (columns 3–5, before applying corrections for extinction and reddening), EW(Li) values reported in the GESiDR5 catalogue (column 6), and our analysis in Section 3.2 (column 7) and the signal-to-noise ratio of the GESiDR5 spectra.

Gaia DR2	P_{3D}	G	$G - J$	$G - K_s$	EW(Li)DR5	EW(Li)RJJ	SNR
3104419133401411840	0.999	11.6590 ± 0.0003	0.8930 ± 0.0240	1.1990 ± 0.0190	118 ± 3	+103.3 ± 11.2	181.5
3104457096612037504	0.998	12.1306 ± 0.0008	1.0046 ± 0.0300	1.3266 ± 0.0320	170 ± 9	+148.8 ± 5.7	177.2
3104435346901124992	1.000	12.0718 ± 0.0025	1.0608 ± 0.0230	1.4228 ± 0.0230	184 ± 6	+175.3 ± 5.1	195.9
3104454347832973696	0.998	12.3488 ± 0.0006	1.0748 ± 0.0260	1.4268 ± 0.0230	157 ± 3	+139.0 ± 3.7	153.3
3104532761057366016	1.000	12.1121 ± 0.0010	0.9961 ± 0.0290	1.4551 ± 0.0230	197 ± 4	+177.9 ± 3.7	133.8
3104339964265249536	1.000	12.1526 ± 0.0005	1.1186 ± 0.0260	1.5536 ± 0.0230	155	+145.0 ± 3.8	121.5
3104494724825684608	0.999	12.3779 ± 0.0025	1.3749 ± 0.0270	1.8639 ± 0.0260	257	+233.7 ± 6.6	134.6
3104336562651152128	0.999	12.7301 ± 0.0019	1.3470 ± 0.0260	1.8920 ± 0.0240	292 ± 4	+272.5 ± 7.4	122.6
3104345255664954368	0.982	12.2941 ± 0.0035	1.3761 ± 0.0230	1.9231 ± 0.0230	289 ± 4	+276.1 ± 10.2	136.6
3104341858349761152	0.999	12.8421 ± 0.0024	1.4621 ± 0.0240	2.0541 ± 0.0230	316 ± 5	+273.2 ± 5.7	88.2
3104444868845867264	0.996	13.5797 ± 0.0047	1.6617 ± 0.0260	2.3297 ± 0.0300	386 ± 6	+354.4 ± 7.2	76.3
3104535784714244480	1.000	13.9327 ± 0.0015	1.7447 ± 0.0340	2.4927 ± 0.0300	363 ± 4	+322.7 ± 3.8	91.0
3104605191385258112	1.000	14.4590 ± 0.0024	2.0940 ± 0.0260	2.9220 ± 0.0240	357 ± 7	+315.4 ± 6.3	48.5
3104245543704247168	1.000	14.8786 ± 0.0028	1.7788 ± 0.0011	3.1886 ± 0.0240	478 ± 8	+424.6 ± 10.8	51.6
3104342579904273152	0.987	14.5603 ± 0.0018	2.4343 ± 0.0260	3.3093 ± 0.0230	354 ± 13	+289.4 ± 12.8	32.2
3104535990872706304	1.000	15.3370 ± 0.0017	2.4742 ± 0.0010	3.3220 ± 0.0190	122 ± 6	+36.6 ± 11.7	29.0
3104245857239589632	1.000	15.3893 ± 0.0035	2.1241 ± 0.0012	3.3253 ± 0.0230	89 ± 7	+2.0 ± 5.1	83.2
3104431812145190272	1.000	15.3449 ± 0.0023	2.1768 ± 0.0012	3.3389 ± 0.0240	136 ± 22	+85.5 ± 9.4	37.2
3104235892915628416	1.000	15.5812 ± 0.0011	2.3148 ± 0.0012	3.3492 ± 0.0230	120 ± 11	+25.5 ± 7.1	49.1
3104529973619388672	1.000	15.5582 ± 0.0013	2.5955 ± 0.0011	3.3752 ± 0.0230	371 ± 23	+306.7 ± 9.6	46.4
3104238950932224512	1.000	15.4832 ± 0.0021	2.3162 ± 0.0012	3.3852 ± 0.0230	161 ± 13	+97.8 ± 8.2	44.8
3104246681873275008	1.000	15.7425 ± 0.0014	2.3493 ± 0.0013	3.3855 ± 0.0260	75	− 4.9 ± 12.5	37.5
3104323029213231488	1.000	15.4756 ± 0.0018	2.4003 ± 0.0011	3.3956 ± 0.0240	128 ± 12	+41.0 ± 8.2	47.0
3104601995929583360	1.000	15.6269 ± 0.0015	2.6373 ± 0.0012	3.4679 ± 0.0270	133 ± 10	+4.8 ± 15.3	20.3
3104431949584129280	1.000	15.7826 ± 0.0023	2.4707 ± 0.0013	3.4706 ± 0.0240	118 ± 14	− 4.5 ± 9.6	45.3
3104446037076422912	1.000	14.8382 ± 0.0011	2.5962 ± 0.0260	3.5042 ± 0.0210	66	+261.9 ± 27.4	33.6
3104534960080775040	1.000	15.1646 ± 0.0017	2.6096 ± 0.0240	3.5326 ± 0.0230	95 ± 10	− 4.8 ± 7.9	55.6
3104528328651278208	0.987	15.7663 ± 0.0009	2.4520 ± 0.0013	3.5733 ± 0.0260	94 ± 10	− 16.6 ± 17.7	28.7
3104558732721761920	0.999	16.2700 ± 0.0025	2.7422 ± 0.0016	3.5910 ± 0.0260	121 ± 6	− 22.6 ± 14.0	29.9
3104214521158310144	0.999	16.1659 ± 0.0026	2.7343 ± 0.0014	3.6019 ± 0.0270	1	− 31.3 ± 16.7	14.8
3104432671138660480	1.000	16.3635 ± 0.0014	2.7411 ± 0.0015	3.6175 ± 0.0300	132	− 37.5 ± 18.3	28.3
3104225997310909696	0.999	16.3812 ± 0.0016	2.9444 ± 0.0014	3.6601 ± 0.0290	87 ± 13	− 14.5 ± 21.8	15.0
3104528466090065024	1.000	16.2735 ± 0.0021	2.8704 ± 0.0013	3.6674 ± 0.0230	52 ± 11	− 16.4 ± 18.2	25.5
3104455417284845440	1.000	15.6339 ± 0.0022	2.7469 ± 0.0010	3.6759 ± 0.0240	165 ± 13	+29.2 ± 16.2	20.8
3104173525693960704	0.999	16.2391 ± 0.0020	2.8244 ± 0.0013	3.6881 ± 0.0260	134 ± 16	− 10.0 ± 27.5	11.9

Table C1 – *continued*

Gaia DR2	P_{3D}	G	$G - J$	$G - K_s$	EW(Li)DR5	EW(Li)RJJ	SNR
3104605019586592256	1.000	16.2785 ± 0.0012	2.8393 ± 0.0015	3.6885 ± 0.0240	153 ± 19	−25.5 ± 18.7	10.9
3104454901887364736	0.999	16.2260 ± 0.0024	2.8556 ± 0.0013	3.6940 ± 0.0350	155 ± 22	+4.4 ± 26.5	13.2
3104506922532654848	0.996	15.9396 ± 0.0024	3.0363 ± 0.0010	3.7396 ± 0.0260	10	−1.3 ± 48.9	17.5
3104474108982725888	1.000	16.6415 ± 0.0026	2.9218 ± 0.0016	3.7435 ± 0.0300	125 ± 10	+27.3 ± 17.1	19.9
3104434286046639744	0.998	16.4142 ± 0.0033	2.9474 ± 0.0014	3.7642 ± 0.0230	100 ± 20	+2.8 ± 12.4	30.7
3104528289992577152	0.998	17.0776 ± 0.0019	2.9760 ± 0.0020	3.7940 ± 0.0033	84 ± 21	+7.8 ± 19.3	19.8
3104226306548544128	0.997	15.9935 ± 0.0023	2.8783 ± 0.0011	3.7955 ± 0.0260	77	−45.4 ± 23.8	30.1
3104425588734811648	0.998	16.9580 ± 0.0018	2.9737 ± 0.0019	3.7990 ± 0.0031	99 ± 21	+14.8 ± 33.6	10.5
3104243589496954624	1.000	16.4457 ± 0.0023	2.8700 ± 0.0015	3.8087 ± 0.0330	112 ± 17	−3.0 ± 10.8	32.1
3104440814396743552	0.999	16.9054 ± 0.0026	2.9961 ± 0.0018	3.8128 ± 0.0029	65 ± 13	−38.8 ± 19.6	16.6
3104454317773799808	0.999	17.1865 ± 0.0017	3.0133 ± 0.0021	3.8266 ± 0.0035	79	+3.3 ± 36.3	6.0
3104506437197663232	1.000	16.9640 ± 0.0017	3.0283 ± 0.0018	3.8482 ± 0.0030	176	+28.5 ± 39.3	9.0
3104246578794084608	0.999	17.2219 ± 0.0016	3.0701 ± 0.0021	3.8646 ± 0.0035	76	−68.3 ± 42.5	8.2
3104582376519289600	0.999	17.0763 ± 0.0026	3.0403 ± 0.0022	3.8652 ± 0.0035	107 ± 17	−42.2 ± 29.8	12.2
3104240840717772288	0.999	17.0603 ± 0.0015	3.0392 ± 0.0019	3.8654 ± 0.0031	66	−13.1 ± 27.7	12.5
3104536952945322880	1.000	16.4957 ± 0.0026	3.0116 ± 0.0014	3.8657 ± 0.0260	103 ± 9	+14.4 ± 14.5	21.8
3104530424595112576	1.000	16.4198 ± 0.0035	3.0508 ± 0.0013	3.8858 ± 0.0300	80 ± 9	+9.1 ± 20.5	22.8
3104440676957804672	0.998	16.6423 ± 0.0029	3.0207 ± 0.0015	3.8893 ± 0.0300	67 ± 11	−3.1 ± 20.7	19.2
3104438787171978624	1.000	16.7697 ± 0.0037	3.0383 ± 0.0016	3.8907 ± 0.0320	134	−2.7 ± 16.0	20.4
3104331722226892800	0.998	17.4389 ± 0.0017	3.1217 ± 0.0023	3.9154 ± 0.0039	230	−4.3 ± 51.2	6.4
3104425970989680512	0.994	17.4495 ± 0.0016	3.1134 ± 0.0023	3.9295 ± 0.0040	98	−50.7 ± 46.8	10.4
3104505857380683776	0.999	16.7492 ± 0.0012	3.1061 ± 0.0015	3.9362 ± 0.0270	232	+33.8 ± 45.5	9.5
3104504341253607552	0.998	17.2799 ± 0.0014	3.1121 ± 0.0021	3.9366 ± 0.0035	117 ± 33	+40.6 ± 47.5	7.2
3104331477410631552	0.999	17.8006 ± 0.0024	3.1594 ± 0.0029	3.9812 ± 0.0049	189	+46.3 ± 45.5	7.2
3104341136795325312	0.977	16.6180 ± 0.0011	3.1559 ± 0.0014	4.0120 ± 0.0260	142	−57.9 ± 32.3	20.3
3104551414093862400	0.993	18.0674 ± 0.0027	3.2488 ± 0.0032	4.0461 ± 0.0058	82	+49.7 ± 77.5	3.3
3104423668887274496	0.997	17.7533 ± 0.0041	3.2266 ± 0.0026	4.0543 ± 0.0046	283	−308.6 ± 175.7	3.4
3104434625346741504	0.997	18.1226 ± 0.0032	3.2395 ± 0.0035	4.1058 ± 0.0058	245	−64.6 ± 41.8	6.6
3104214482502076672	0.999	18.2245 ± 0.0028	3.2967 ± 0.0034	4.1080 ± 0.0062	301	+101.6 ± 69.9	4.6
3104455619144457600	0.952	18.6173 ± 0.0036	3.3926 ± 0.0043	4.1292 ± 0.0087		+550.9 ± 235.3	1.7
3104438061320152576	0.997	18.2611 ± 0.0025	3.3256 ± 0.0035	4.1337 ± 0.0063	301	+26.3 ± 163.6	2.3
3104329999947214336	0.999	18.2442 ± 0.0030	3.3485 ± 0.0034	4.1557 ± 0.0062	16	−99.8 ± 61.7	4.7
3104328045734809088	0.998	18.4632 ± 0.0035	3.3488 ± 0.0040	4.1726 ± 0.0072	371	+43.5 ± 113.2	3.6
3104212558354814464	0.988	17.6424 ± 0.0021	3.3891 ± 0.0022	4.1906 ± 0.0037	340	+158.1 ± 47.2	6.6
3104243756998337152	0.989	18.3675 ± 0.0034	3.3856 ± 0.0036	4.2223 ± 0.0065	118	+161.3 ± 126.1	2.8
3104434316109083136	0.999	18.2833 ± 0.0031	3.4164 ± 0.0033	4.2395 ± 0.0059	319	+11.2 ± 107.9	4.2
3104433869432346240	0.997	17.6949 ± 0.0019	3.4324 ± 0.0022	4.2560 ± 0.0037	377	+159.6 ± 46.3	7.2
3104243860077501056	0.993	18.7621 ± 0.0043	3.4224 ± 0.0046	4.2576 ± 0.0087		+538.5 ± 182.7	1.5
3104431124950743936	0.988	17.8219 ± 0.0037	3.4325 ± 0.0024	4.2612 ± 0.0041	239 ± 30	+515.2 ± 97.0	6.2
3104561893816700800	0.990	18.9278 ± 0.0046	3.4628 ± 0.0061	4.2892 ± 0.0108	843	+732.7 ± 159.7	2.5
3104426482088556800	0.995	18.7511 ± 0.0041	3.5029 ± 0.0044	4.3109 ± 0.0083	342 ± 41	+328.1 ± 100.3	3.0
3104341132499390336	0.982	19.1105 ± 0.0055	3.5576 ± 0.0054	4.3786 ± 0.0106	827	+318.0 ± 242.0	1.3
3104216204782370048	0.994	16.3720 ± 0.0093	3.4406 ± 0.0010	4.3980 ± 0.0240	134 ± 14	+63.4 ± 25.9	15.2
3104534715263592192	0.991	18.5571 ± 0.0032	3.5934 ± 0.0036	4.4142 ± 0.0065	675	+470.9 ± 166.4	1.9
3104340891981168128	0.989	19.2257 ± 0.0045	3.6745 ± 0.0054	4.5418 ± 0.0100	756	+511.2 ± 240.1	1.6

This paper has been typeset from a $\text{\TeX}/\text{\LaTeX}$ file prepared by the author.